Photoelectrochemical removal of chlorfenvinphos by using WO_3 nanorods: influence of annealing temperature and operation pH

Fernández-Domene, R.M.; Roselló-Márquez, G., Sánchez-Tovar, R.; Lucas-Granados, B.; García-Antón, J.

Ingeniería Electroquímica y Corrosión (IEC). Instituto Universitario de Seguridad Industrial, Radiofísica y Medioambiental (ISIRYM). Universitat Politècnica de València. Camino de Vera s/n, 46022 Valencia, Spain. Tel. 34-96-387 76 32, Fax. 34-96-387 76 39. E-mail: *jgarciaa@iqn.upv.es (J. García-Antón).*

ABSTRACT

A visible-light driven photoelectrochemical degradation process has been applied to a solution polluted with the organophosphate insecticide chlorfenvinphos. Different WO_3 nanosheets/nanorods have been used as photoanodes. These nanostructured electrodes have been fabricated by anodization of tungsten and, subsequently, they have been subjected to a thermal treatment (annealing). The combined influence of annealing temperature (400º C and 600º C) and operation pH (1 and 3) on the photoelectrocatalytic behavior of these nanorods has been examined through a statistical analysis. Morphological, structural and photoelectrochemical characterizations have also been carried out. The chlorfenvinphos degradation efficiency depended both on annealing temperature and, specially, operation pH. At pH 1 and using an annealing temperature of 600º C, chlorfenvinphos has been effectively degraded following pseudo-first order kinetics with a coefficient of 7.8×10^{-3} min^{-1}, and notably mineralized (more than 65% of Total Organic Carbon decrease).

Keywords: Photoelectrochemical degradation; WO_3 nanorods; anodization; chlorfenvinphos; regression model.

1. INTRODUCTION

Organophosphate insecticides constitute a large group of synthetic organic compounds, highly toxic in many cases, whose precedent are the so-called “nerve gases” or “nerve agents” (sarin, tabun, soman, etc.) which were developed after World War II. The properties of these compounds made them very useful against insect plagues, so they have been used since then, as active ingredients, in many commercial formulations [1].

Organophosphate insecticides, such as parathion, diazinon or chlorfenvinphos, have been or are still widely used in agriculture, homes, gardens and veterinary practices. Once these insecticides have entered the organism of insects (and other animals, including human beings), cholinesterase-type enzymes, especially acetylcholinesterase, become their target molecules. This enzyme has a prominent physiological function in the nervous system. Transmission of nerve impulses from nerve fibers to smooth and skeletal muscle cells is inhibited by the reaction with organophosphate pesticides through phosphorylation, hence poisoning the organism [2]. Apart from their toxicity, these insecticides are also very persistent in the environment, with reported half-lives of 100-200 days in water [3].

Chlorfenvinphos –or 2-chloro-1-(2,4 dichlorophenyl) vinyl diethyl phosphate– is commonly used for protection against insects in agriculture and to control insect pests (flies, fleas, ticks, mites, etc.) on farm animals [4]. According to the European Chemical Agency, this insecticide is fatal if swallowed, toxic in contact with skin and very toxic to aquatic organisms with permanent effects [5].

This insecticide has been found in several aquifers (rivers, lagoons, ...), as well as in effluents from sewage treatment plants [3, 6-24]. Chlorfenvinphos can enter the environment from runoff due to rainfall, leaching from hazardous waste sites through large regions of soil and eventually reaching water resources, including underground wells [4], where it may threaten the aquatic environment and human health. The detection of this insecticide has been especially noticeable in the Mediterranean area, in spite of chlorfenvinphos being withdrawn from the EU [25].

The removal of hazardous pesticides from polluted surface waters and wastewaters cannot be efficiently performed by biological techniques, since they are toxic for microorganisms, thus hindering biodegradation. Other methods, based on the generation of the very oxidizing hydroxyl radicals, called Advanced Oxidation Processes (AOPs), have been used to remove chlorfenvinphos from aqueous solutions [10, 26-34]. However, most of the used methods involve high energies (gamma irradiation, low pressure UV photolysis) or require the use of expensive additional reagents (H_2O_2, O_3, etc.) which make them not suitable to treat large volumes of water. Heterogeneous photocatalysis (PC) using semiconductor oxides could be an alternative, but the efficiencies of these processes are frequently limited by the fast recombination of photogenerated electron-hole pairs (e^-–h^+), due to the absence of an electric field inside the semiconductor [35, 36]. This problem can be overcome by using photoelectrocatalysis (PEC), where an external low bias is applied to the photoelectrocatalyst to help separating e^-–h^+, hence enhancing the overall efficiency [35]. To our knowledge, no photoelectrocatalytic process has been reported yet in the literature for chlorfenvinphos degradation.Tungsten trioxide (WO_3) is a good candidate to be used as semiconductor photoanode in PEC due to its good properties, especially its

photoelectrocatalytic properties [37]. No published study where WO_3 was used as (photo)catalyst for chlorfenvinphos degradation has been found.

The aim of this study is to investigate the influence of two important parameters, annealing temperature and operation pH, on the photoelectrocatalytic performance of WO_3 nanostructures, through a statistical analysis. Solutions of chlorfenvinphos were degraded using the WO_3 photoanodes under visible-light illumination. Before the degradation tests, these photoanodes were morphological, structural and electrochemically characterized through Field Emission Scanning Electronic Microscopy (FESEM), Raman spectroscopy and Electrochemical Impedance Spectroscopy (EIS).

2. EXPERIMENTAL PROCEDURE

2.1. Nanostructures fabrication

Nanostructured WO_3 photoanodes were fabricated by anodization of tungsten cylinders (8 mm in diameter) under hydrodynamic conditions using a rotating disk electrode (RDE) at 375 rpm. Before anodization, tungsten cylinders were wet abraded with 220, 500 and 4000 grit SiC papers, rinsed with distilled water and dried with compressed air. The tunsgten cylinders were coated with teflon in order to expose only a circular area of 0.5 cm^2 to the electrolyte. The anodization electrolyte was a 1.5 M H_2SO_4 + 0.05 M H_2O_2 solution. A potential difference of 20 V was imposed between the anode (tungsten) and the cathode (platinum mesh). The temperature of the electrolyte (50º C) was controlled by a thermostatic bath.

After anodization, thin slices containing the formed nanostructures were cut from the tungsten cylinders and subjected to a thermal treatment for 4 h using two different annealing temperatures: 400º C and 600º C, at a heating rate of 15º C min^{-1}. This thermal treatment was performed in order to obtain dehydrated and crystalline WO_3 nanostructures.

2.2. Sample characterization

Morphology of WO_3 nanostructures was characterized through FESEM, using an acceleration voltage of 3 kV, while their composition and crystalline structure were studied through Raman spectroscopy, using a Raman Confocal Laser Microscope with a neon laser wavelength of 632 nm and a power of 420 μW. Energy Dispersive X-ray spectroscopy (EDX) was also used to verify the chemical composition of the WO_3 nanostructures, applying an accelerating voltage of 20 kV. Finally, EIS experiments were performed under illumination conditions (using 420 nm light) in order to investigate the photoelectroactivity of the samples. For EIS measurements, a three-electrode transparent quartz cell was used, with the nanostructures acting as working electrodes, a platinum tip acting as a counter electrode and a Ag/AgCl (3M KCl) reference electrode. An Autolab PGSTAT302N potentiostat was used to apply an external polarization of 1 V and to record the impedance values. The frequency range varied from 10 kHz to 10 mHz, using a sinusoidal potential perturbation of 10 mV peak to peak.

2.3. Photoelectrocatalytic degradation experiments

The pesticide used in this study was chlorfenvinphos (SigmaAldrich Pestanal, analytical standard). Chlorfenvinphos solutions were prepared from a stock solution of 100 ppm, which was stored at 4º C in the absence of light. Degradation tests were performed at 20º C using the same electrode configuration explained above for the EIS experiments, applying an external potential difference of 1 V to the system and under constant magnetic stirring. The initial concentration of chlorfenvinphos was 20 ppm and the treated volume was 14 mL. Two different operation pH values were used: pH 1 and pH 3, by adding the necessary amount of H_2SO_4. Irradiation was provided by a 1000 W Xe light source, selecting a visible wavelength of 420 nm. The light power density was 100 mW cm^{-2}.

2.4. Analytical methods

The pesticide concentration variation with time was monitored by UV spectrophotometry, measuring the absorbance within a range of wavelengths (190-320 nm). Liquid samples of 4 mL were withdrawn from the quartz reactor every 30 min to measure their absorbance. After measurements, these samples were returned to the reactor to continue with the degradation. The degradation tests lasted 360 min.

Mineralization of chlorfenvinphos after 360 min of degradation was monitored by measuring the Total Organic Carbon (TOC) of the treated solutions using a Shimadzu TOC-L analyzer.

3. RESULTS AND DISCUSSION

3.1. Nanostructures characterization

As explained above in the experimental section, WO_3 nanostructures were exposed to thermal treatment for 4 h in order to obtain dehydrated and crystalline structures. To study the influence of annealing temperature on the photoelectrocatalytic behavior of the nanostructures, two different values were selected: 400º C and 600º C.

The morphological characterization of the nanostructures was performed through FESEM. **Figure 1a** and **Figure 1b** show different images of the formed nanostructures after the annealing treatment. It can be observed that in both cases, very small nanorods or nanosheets were formed on the electrode surface forming a kind of spongy layer. The very small size of these nanostructures and the way they aggregate can be associated with the tendency of the bidentate O_2^{2-} ligand to form very strong bonds with tungsten during anodization, which made the growth of the nanostructures difficult during their synthesis [38]. However, annealing temperature had an important influence on the nanostructures morphology. At 600º C, nanorods were much more defined, probably implying a higher degree of dehydration of the nanostructure. The cross sections of the nanostructures are shown as insets in **Figure 1a** and **Figure 1b**. It can be seen that these minuscule nanorods or nanosheets aggregated in many layers. From different cross-sectional images, the thickness of the nanostructured layer was determined to be 2.1 ± 0.3 μm for the nanostructure annealed at 400º C, and 1.7 ± 0.2 μm at 600º C. This

slightly decrease in thickness at the highest temperature may also be a consequence of a higher degree of dehydration, resulting in a shrinking of nanorods.

A current density transient recorded during the 4 h of anodization is presented in **Figure 1c**, with the aim of studying the formation mechanism of the WO_3 nanostructures used in this work. Just after applying the 20 V of cell potential difference, a steep decrease in current density was observed. This decrease was caused by the formation of a compact WO_3 layer on the exposed surface, which blocked the tungsten surface, according to the following reaction:

$$W + 3H_2O \rightarrow WO_3 + 6H^+ + 6e^- \quad \textbf{(1)}$$

After that decrease, current density started to increase until about 2500 s, which was related to the dissolution of the aforementioned compact WO_3 layer due to the interaction between the peroxo ligand (O_2^{2-}) and WO_3. This reaction resulted in the formation of peroxotungstates and peroxotungstic acids, of which the species $[W_2O_{11}]^{2-}$ seems to be predominant [38]:

$$2WO_3 + 4H_2O_2 \rightarrow [W_2O_{11}]^{2-} + 2H^+ + 3H_2O \quad \textbf{(2)}$$

When supersaturation conditions were achieved near the electrode due to the continuous release of peroxotungstates and peroxotungstic acids, these species precipitated on the tungsten surface in the form of tungstic acids ($WO_3 \cdot H_2O$ and $WO_3 \cdot 2H_2O$). Besides, $W_2O_{11}^{2-}$ can also decompose into solid WO_3, according to:

$$[W_2O_{11}]^{2-} + 2H^+ \rightarrow 2WO_3 + 2O_2 + H_2O \quad \textbf{(3)}$$

Precipitation of tungstic acids and WO_3 in the form of nanostructures resulted in a constant decrease of current density, which reached low values at the end of the 4 h of anodization, similar to those observed at the beginning of the process.

In order to confirm the higher dehydration degree experimented by the nanostructure annealed at 600º C, Raman spectroscopy was used. **Figure 2a** shows Raman spectra of the WO_3 nanostructures after annealing at 400º C and 600º C. Characteristic monoclinic WO_3 peaks were clearly seen in both spectra (190 cm^{-1}, 275 cm^{-1}, 715 cm^{-1} and 807 cm^{-1}) [38-43]. However, there are two evident differences between both plots. For the sample annealed at 400º C, a broad and low-intensity band centered at ~950 cm^{-1} can be observed, while this band is absent for the sample annealed at 600º C. This band has been traditionally associated with amorphous $WO_3 \cdot xH_2O$ [40-44]. This result indicate that the nanostructure treated at 400º C was somewhat hydrated whereas at 600º C dehydration was complete. Moreover, a peak at 330 cm^{-1} appeared for the sample annealed at 600º C, while this peak was barely visible for the sample treated at 400º C. This peak has also been related to crystalline monoclinic WO_3 [39-43]. Consequently, it can be concluded that the degrees of crystallinity and dehydration of the WO_3 nanostructure annealed at 600º C were higher than those for the sample annealed at 400º C. In **Figure 2b**, an EDX spectrum of the WO_3 nanostructure annealed at 400º is presented by way of illustration. Peaks of tungsten and oxygen can clearly be seen, confirming that WO_3 was formed.

With the aim of investigating the influence of annealing temperature on the photoelectrochemical activity of the nanostructures, EIS measurements under a 420 nm

light were performed. Nyquist and Bode-phase plots for the WO_3 nanostructures are shown in **Figure 3**. Two semicircles can be observed in each Nyquist plot (**Figure 3a**), one at high frequencies and the other at intermediate and low frequencies. The amplitude of these semicircles was visibly lower for the sample annealed at 600º C, which means that charge transfer processes under illumination were, in general, favored at this nanostructure (lower charge transfer resistances). Bode phase plots (**Figure 3b**) displayed two clear peaks (400º C) or one broad peak (600º C), which can be the result of two overlapping peaks. These results indicate that, at least, an electric equivalent circuit with two time constants should be used to fit the EIS results. To quantify charge transfer resistances, the electric equivalent circuit shown in **Figure 3c** has been used. In this circuit, R_S represents the electrolyte resistance, the R_1-CPE_1 time constant is related to charge-transfer processes at the nanostructure/electrolye interface and the R_2-CPE_2 time constant is related to a compact WO_3 layer formed beneath the nanorods. Constant phase elements (CPEs) have been used instead of capacitors to take the non-ideality of the system into account. Charge-transfer resistance values are shown in **Table 1**. Both R_1 and R_2 were lower for the nanostructure annealed at 600º C, confirming that charge-transfer processes were enhanced for this nanostructure under illumination. These results can be directly associated with the higher degree of crystallinity of this nanostructure, which improved electrochemical and photoelectrochemical interfacial phenomena.

3.2. Photoelectrocatalytic degradation of chlorfenvinphos and mineralization degree

Apart from annealing temperature (400º C and 600º C), the operation pH was also modified between two levels: pH 1 and pH 3. **Figure 4** shows the temporal evolution of chlorfenvinphos UV absorbance spectra for the different experimental conditions. The initial chlorfenvinphos spectrum showed two clear absorbance peaks centered at 205 nm and 245 nm. The second peak (245 nm) has been related in the literature to the π–π* transition of the aromatic ring and it is the peak normally used to track the decomposition of this organophosphate pesticide [32, 45]. It can be observed from **Figure 4** that the intensity of both peaks decreased with irradiation time, regardless of the experimental conditions. However, this decrease was much more evident for the experiments carried out at pH 1. After 360 min of degradation and at pH 1, the absorbance peak centered at 245 nm completely disappeared for the nanostructure annealed at 600º C and took values close to zero for the nanostructure annealed at 400º C (but was not totally absent). Moreover, this peak was not displaced to lower wavelengths during the degradation reaction, indicating that intermediate compounds such as 2,4-dichlorophenol or 2,4-dichlorobenzoic acid were not formed. The formation of these compounds would imply a red-shift of this peak [32]. On the other hand, absorbance between 200-220 nm took values higher than zero. These results mean that (1) degradation of chlorfenvinphos likely took place through the aromatic ring opening, and (2) this degradation resulted in the formation of other intermediate compounds whose molecules absorbed light in the wavelength range between 200 nm and 220 nm. Nevertheless, further analytical work is necessary to propose a complete degradation mechanism for chlorfenvinphos. This study will be developed in future works.

The decrease of the absorbance at 245 nm was related to the concentration of chlofenvinphos by using a calibration line. The degradation efficiency was determined according to the following equation:

$$\eta = \frac{C_0 - C(t)}{C_0} \times 100 \quad \textbf{(1)}$$

where C_0 is the initial chlorfenvinphos concentration and $C(t)$ is chlorfenvinphos concentration at different times. Degradation efficiencies are shown in **Figure 5a**. At pH 3, little differences were observed between WO_3 samples, and degradation efficiencies of 37% (600º C) and 34% (400º C) were obtained. At pH 1, although differences were not marked, the WO_3 nanostructure annealed at 600º C displayed the best degradation efficiency (95% vs. 91% for the nanostructure annealed at 400º C).

Pseudo-first order kinetic coefficients for chlorfenvinphos degradation are presented in **Table 2**, as well as the respective correlation coefficients (R^2) for the linearization. At 600º C, higher kinetic coefficients were obtained, regardless of the operation pH. On the other hand, at pH 1, these values were much higher, especially at 600º C, which is consistent with the previous results. As stated in the introduction, this is the first study involving photoelectrocatalytic degradation of chlorfenvinphos. Therefore, kinetic coefficients obtained here cannot be compared with other coefficients obtained under similar experimental conditions. In order to make a rough comparison, a study about photocatalytic degradation of chlorfenvinphos by using suspensions of TiO_2 will be used [29]. In that work, 200 mg L^{-1} of TiO_2 photocatalyst were used, in a solar reactor with a total volume between 72-80 L and using a solar collector composed of four compound parabolic collector units. The obtained pseudo-first order kinetic coeffient

for chlorfenvinphos degradation was 0.014 min^{-1}, higher than the 0.0078 min^{-1} obtained in this work. However, to adequately compare these kinetic coefficients, experimental conditions should be similar, and the solar pilot plant used by Malato et al. is very different from the laboratory degradation system used in this work.

Mineralization degree of chlorfenvinphos was determined through the analysis of total organic carbon. TOC values for all different conditions, together with the percentage of TOC decrease, are shown in **Figure 5b**. Initial values are also shown for comparison. At pH 3, the maximum TOC decrease was obtained for the nanostructure annealed at 600º C (19 %), while for the nanostructure annealed at 400º C, that reduction was of 16.9 %. At pH 1, TOC values significantly decreased, reaching a 65.3 % of TOC reduction for the nanostructure treated at 600º C (and 60.5 % for sample annealed at 400º C).

Consequently, in accordance with the previous results, it can be concluded that WO_3 nanostructures used in the present study are efficient for their use as photoanodes in the PEC degradation of chlorfenvinphos.

3.3. Regression analysis: influence of annealing temperature and operation pH

With the purpose of finding the relationship between the two factors studied in this work (annealing temperature *T* and operation pH) on the photoelectrocatalytic behavior of WO_3 nanostructured photoanodes, a regression analysis was performed. The kinetic coefficient (*k*) was used as response variable and the purpose was to maximize it. A 2^2 factorial design was selected, since it combines simplicity and effectiveness. The equation of the regression model is:

$$k = \beta_0 + \beta_1 \cdot T + \beta_2 \cdot pH + \beta_3 \cdot T \cdot pH \quad \textbf{(2)}$$

According to ANOVA, a statistically significant result is obtained when the *p*-value is lower than the stipulated significance level. In this case, this upper limit was set at 0.05. Therefore, for a given factor, *p*-values lower than 0.05 mean that this factor had a significant influence on the response variable, an effect that cannot be explained by simple random chance. In **Table 3**, *p*-values for each factor and for the interaction between them, as well as the regression coefficients β_0, β_1, β_2 and β_3, are shown (the parameter β_0, which is the expected value of *k* when *T* and *pH* are zero, has no physical meaning, but its value is also shown in Table 3 to provide a complete version of the regression model). It can be seen that all *p*-values are lower than 10^{-4}, which indicates that the effects of both factors and the interaction were significant.

The main effects and interaction plots are shown in **Figure 6**. Lines observed in the main effects plot (**Figure 6a**) indicate the estimated changes in the kinetic coefficient when each factor is moved from its lowest level to its highest level, setting the other factor at an intermediate value between the lowest and highest level (i.e. setting *T* = 500º C and pH = 2). It is clear that the factor with the most significant effect was operation pH, which has to be set at its lowest limit (pH 1) in order to maximize the kinetic coefficient (**Figure 6a**). The influence of annealing temperature was smaller, although it was also found to be significant: to maximize *k*, annealing temperature must be set at its maximum value (600º C) (**Figure 6a**). Concerning the interaction between both factors, its effect was also significant, since no parallel lines are observed in

Figure 6b. From these results, it can be concluded that optimum values are pH 1 and 600º C.

The strong influence of operation pH can be explained by taking into account the chemistry of tungsten species. WO_3 is chemically stable in acidic solutions. In fact, precipitation of hydrated forms of WO_3 (known as tungstic acids), which was the formation mechanism of nanostructures used in this work, is achieved at pH of 1 or lower [46]. Hence, a better photoelectrochemical performance of WO_3 photoelectrodes is expected in acidic environments. On the other hand, the higher degrees of dehydration and crystallinity of nanostructures annealed at 600º C (see **Figure 2)** would explain the enhancement of degradation efficiency of these samples in comparison with samples treated at 400º C.

4. CONCLUSIONS

Very small nanorods or nanosheets were formed by electrochemical anodization of tungsten, regardless of the annealing temperature. Nevertheless, at 600º C, nanorods were much more defined due to a higher degree of dehydration and crystallinity of the nanostructure. Hence, annealing temperature had an important influence on the nanostructures morphology.

The higher degree of dehydration and crystallinity of nanorods obtained at 600º C was confirmed by Raman spectroscopy. A peak directly related to amorphous and hydrated

WO_3 was observed for the sample annealed at 400º C, but not for the sample annealed at 600º C.

Charge-transfer resistances under illumination were lower for the nanostructure fabricated at 600º C. This result has been associated with the higher degree of crystallinity of this nanostructure, which improved electrochemical and photoelectrochemical interfacial phenomena.

The UV absorbance peak associated with the aromatic ring of chlorfenvinphos (at 245 nm) decreased with irradiation time for all experimental cases. However, this decrease was much more pronounced at pH 1 than at pH 3. The temporal evolution of this peak indicated that degradation likely proceeded through the cleavage of the aromatic ring, rather than through the formation of intermediate compounds such as 2,4-dichlorophenol or 2,4-dichlorobenzoic acid, although future investigations are necessary to confirm this preliminary results.

More than 65% of the initial chlorfenvinphos was mineralized after 360 min of degradation reaction for the nanostructure annealed at 600º C and under an operation pH of 1.

A statistical analysis has shown that both annealing temperature and operation pH, as well as their interaction, had a significant effect on the pseudo-first order kinetic coefficient, especially the operation pH. In order to maximize this coefficient, annealing temperature must be fixed at its highest value (600º C) and pH at its lowest value (pH 1). The important influence of operation pH can be explained by taking into account the

chemical and photoelectrochemical stability of WO_3 in highly acidic environments, which enhanced the photoelectrochemical performance of WO_3 photoelectrodes. On the other hand, the higher degrees of dehydration and crystallinity of nanostructures annealed at 600º C explained the improvement of degradation efficiency of these samples in comparison with samples treated at 400º C.

Acknowledgements

Authors thank for the financial support to the Ministerio de Economía y Competitividad (Project Code: CTQ2016-79203-R), for its help in the Laser Raman Microscope acquisition (UPOV08-3E-012) and for the co-finance by the European Social Fund. Ramón M. Fernández Domene thanks the UPV for the concession of a post-doctoral grant (PAID-10-17) and Gemma Roselló Márquez also thanks the Generalitat Valenciana for the concession of a pre-doctoral grant (ACIF/2018/159).

REFERENCES

[1] World Health Organization - Regional Office for the Eastern Mediterranean (WHO EMRO). *Nerve gases: Tabun (CAS 77-81-6); Sarin (CAS 107-44-8); Soman (CAS 96-64-0); VX (CAS 50782-69-9) fact sheet* (http://www.emro.who.int/ceha/information-resources/nerve-gas-fact-sheet.html, accessed 9 November 2018).

[2] U.S.Environmental Protection Agency. *Pesticide Poisoning Handbook - Section II Insecticides* (Chapter 5: Organophosphate Insecticides), (https://www.epa.gov/sites/production/files/documents/rmpp_6thed_ch5_organophosphates.pdf; accessed 9 November 2018).

[3] S. B. Lartiges, P. P. Garrigues. Degradation Kinetics of Organophosphorus and Organonitrogen Pesticides in Different Waters under Various Environmental Conditions, Environ. Sci. Technol. 29 (1995) 1246-1254.

[4] U.S.Agency for Toxic Substances and Disease Registry (ATSDR). *Toxicological Profile for Chlorfenvinphos*. 1997.

[5] European Chemicals Agency (ECHA). Chlorfenvinphos Information ((https://echa.europa.eu/substance-information/-/substanceinfo/100.006.758; accessed 9 November 2018).

[6] D. Medina, A. Prieto, G. Ettiene, I. Buscema, d. Abreu, V. Persistence of Organophosphorus Pesticide Residues in Limón River Waters, Bull. Environ. Contam. Toxicol. 63 (1999) 39-44.

[7] H. C. Bailey, J. R. Elphick, R. Krassoi, A. Mulhall, A. J. Lovell, D. J. Slee. Identification of chlorfenvinphos toxicity in a municipal effluent in Sydney, New South Wales, Australia, Environ. Toxicol. Chem. 24 (2009) 1773-1778.

[8] M. Staniszewska, H. Boniecka, A. Gajecka. Organochlorine, Organophosphoric and Organotin Contaminants, Aromatic and Aliphatic Hydrocarbons and Heavy Metals in Sediments of the Ports from the Polish Part of the Vistula Lagoon (Baltic Sea), Soil Sediment Contam. 22 (2013) 151-173.

[9] V. Belenguer, F. Martinez-Capel, A. Masiá, Y. Picó. Patterns of presence and concentration of pesticides in fish and waters of the J+¦car River (Eastern Spain), J. Hazard. Mater. 265 (2014) 271-279.

[10] C. Oliveira, A. Alves, L. M. Madeira. Treatment of water networks (waters and deposits) contaminated with chlorfenvinphos by oxidation with Fenton's reagent, Chem. Eng. J. 241 (2014) 190-199.

[11] E. Silva, M. A. Daam, M. J. Cerejeira. Aquatic risk assessment of priority and other river basin specific pesticides in surface waters of Mediterranean river basins, Chemosphere 135 (2015) 394-402.

[12] F. Kanzari, L. Asia, A. D. Syakti, A. Piram, L. Malleret, G. Mille, P. Doumenq. Distribution and risk assessment of hydrocarbons (aliphatic and PAHs), polychlorinated biphenyls (PCBs), and pesticides in surface sediments from an agricultural river (Durance) and an industrialized urban lagoon (Berre lagoon), France, Environ. Monit. Assess. 187 (2015) 591.

[13] M. Kuzmanovic, J. C. López-Doval, N. De Castro-Català, H. Guasch, M. Petrovic, I. Muñoz, A. Ginebreda, D. Barceló. Ecotoxicological risk assessment of chemical pollution in four Iberian river basins and its relationship with the aquatic macroinvertebrate community status, Sci. Total Environ.540 (2016) 324-333.

[14] C. Cruzeiro, M. Â. Pardal, N. Rodrigues-Oliveira, L. F. Castro, E. Rocha, M. J. Rocha. Multi-matrix quantification and risk assessment of pesticides in the longest river of the Iberian peninsula, Sci. Total Environ. 572 (2016) 263-272.

[15] A. Ccanccapa, A. Masiá, A. Navarro-Ortega, Y. Picó, D. Barceló. Pesticides in the Ebro River basin: Occurrence and risk assessment, Environ. Pollut. 211 (2016) 414-424.

[16] M. I. Pinto, H. D. Burrows, G. Sontag, C. Vale, J. P. Noronha. Priority pesticides in sediments of European coastal lagoons: A review, Mar. Pollut. Bull. 112 (2016) 6-16.

[17] A. Ccanccapa, A. Masiá, V. Andreu, Y. Picó. Spatio-temporal patterns of pesticide residues in the Turia and Júcar Rivers (Spain), Sci. Total Environ. 540 (2016) 200-210.

[18] Y. Xie, J. Wang, Y. Wu, C. Ren, C. Song, J. Yang, H. Yu, J. P. Giesy, X. Zhang. Using in situ bacterial communities to monitor contaminants in river sediments, Environ. Pollut. 212 (2016) 348-357.

[19] C. Corada-Fernández, L. Candela, N. Torres-Fuentes, M. G. Pintado-Herrera, M. Paniw, E. González-Mazo. Effects of extreme rainfall events on the distribution of selected emerging contaminants in surface and groundwater: The Guadalete River basin (SW, Spain), Sci. Total Environ. 605-606 (2017) 770-783.

[20] M. Kuzmanovic, S. Dolédec, N. de Castro-Catala, A. Ginebreda, S. Sabater, I. Muñoz, D. Barceló. Environmental stressors as a driver of the trait composition of benthic macroinvertebrate assemblages in polluted Iberian rivers, Environ. Res. 156 (2017) 485-493.

[21] Z. Tousova, P. Oswald, J. Slobodnik, L. Blaha, M. Muz, M. Hu, W. Brack, M. Krauss, C. Di Paolo, Z. Tarcai, T. B. Seiler, H. Hollert, S. Koprivica, M. Ahel, J. E. Schollée, J. Hollender, M. J. F. Suter, A. O. Hidasi, K. Schirmer, M. Sonavane, S. it-Aissa, N. Creusot, F. Brion, J. Froment, A. C. Almeida, K. Thomas, K. E. Tollefsen, S. Tufi, X. Ouyang, P. Leonards, M. Lamoree, V. O. Torrens, A. Kolkman, M. Schriks, P. Spirhanzlova, A. Tindall, T. Schulze. European demonstration program on the effect-based and chemical identification and monitoring of organic pollutants in European surface waters, Sci. Total Environ. 601-602 (2017) 1849-1868.

[22] N. I. Rousis, R. Bade, L. Bijlsma, E. Zuccato, J. V. Sancho, F. Hernandez, S. Castiglioni. Monitoring a large number of pesticides and transformation products in water samples from Spain and Italy, Environ. Res. 156 (2017) 31-38.

[23] J. A. Pascual Aguilar, V. Andreu, J. Campo, Y. Picó, A. Masiá. Pesticide occurrence in the waters of Júcar River, Spain from different farming landscapes, Sci. Total Environ. 607-608 (2017) 752-760.

[24] S. E. Hook, H. Doan, D. Gonzago, D. Musson, J. Du, R. Kookana, M. J. Sellars, A. Kumar. The impacts of modern-use pesticides on shrimp aquaculture: An assessment for north eastern Australia, Ecotox. Environ. Safe. 148 (2018) 770-780.

[25] Commission Regulation (EC) Nº 2076/2002 of 20 November 2002 (concerning the non-inclusion of certain active substances in Annex I to Council Directive 91/414/EEC and the withdrawal of authorisations for plant protection products containing these substances). (http://eur-lex.europa.eu/legal-content/EN/TXT/HTML/?uri=CELEX:32002R2076&from=EN; accessed 9 November 2018).

[26] M. I. Maldonado, S. Malato, L. A. Pérez-Estrada, W. Gernjak, I. Oller, X. Doménech, J. Peral. Partial degradation of five pesticides and an industrial pollutant by ozonation in a pilot-plant scale reactor, J. Hazard. Mater. 138 (2006) 363-369.

[27] M. I. Maldonado Rubio, W. Gernjak, I. Oller Alberola, J. Blanco Gálvez, P. Fernández-Ibáñez, S. Malato Rodríguez. Photo-Fenton degradation of alachlor, atrazine, chlorfenvinphos, diuron, isoproturon and pentachlorophenol at solar pilot plant, Int. J. Environ. Pollut. 27 (2006) 125-146.

[28] C. F. Gromboni, M. Y. Kamogawa, A. G. Ferreira, J. A. Nóbrega, A. R. Nogueira. Microwave-assisted photo-Fenton decomposition of chlorfenvinphos and cypermethrin in residual water, J. Photochem. Photobiol. A: Chem. 185 (2007) 32-37.

[29] M. I. Maldonado, P. C. Passarinho, I. Oller, W. Gernjak, P. Fernández, J. Blanco, S. Malato. Photocatalytic degradation of EU priority substances: A comparison between TiO_2 and Fenton plus photo-Fenton in a solar pilot plant, J. Photochem. Photobiol. A: Chem. 185 (2007) 354-363.

[30] J. L. Acero, F. J. Real, F. Javier Benitez, A. González. Oxidation of chlorfenvinphos in ultrapure and natural waters by ozonation and photochemical processes, Water Res. 42 (2008) 3198-3206.

[31] N. Klamerth, W. Gernjak, S. Malato, A. Agüera, B. Lendl. Photo-Fenton decomposition of chlorfenvinphos: Determination of reaction pathway, Water Res. 43 (2009) 441-449.

[32] A. Bojanowska-Czajka, A. Galezowska, J. L. Marty, M. Trojanowicz. Decomposition of pesticide chlorfenvinphos in aqueous solutions by gamma-irradiation, J. Radioanal. Nucl. Chem. 285 (2010) 215-221.

[33] S. Sanches, M. T. Barreto Crespo, V. J. Pereira. Drinking water treatment of priority pesticides using low pressure UV photolysis and advanced oxidation processes, Water Res. 44 (2010) 1809-1818.

[34] A. Bojanowska-Czajka, M. Trojanowicz, A. Galezowska, H. Nichipor, Z. Zimek, J. L. Marty, G. Nalecz-Jawecki. Radiolytic Removal of Selected Pesticides From Waters and Waste Using Ionizing Radiation, Sep. Sci. Technol. 45 (2010) 1651-1657.

[35] R. Daghrir, P. Drogui, D. Robert. Photoelectrocatalytic technologies for environmental applications, J. Photoch. Photobio. A 238 (2012) 41-52.

[36] S. Garcia-Segura, E. Brillas. Applied photoelectrocatalysis on the degradation of organic pollutants in wastewaters, J. Photoch. Photobio. C 31 (2017) 1-35.

[37] H. Zheng, J. Z. Ou, M. S. Strano, R. B. Kaner, A. Mitchell, K. Kalantar-zadeh. Nanostructured Tungsten Oxide - Properties, Synthesis, and Applications, Adv. Funct. Mater. 21 (2011) 2175-2196.

[38] M. F. Daniel, B. Desbat, J. C. Lassegues, B. Gerand, M. Figlarz. Infrared and Raman study of WO_3 tungsten trioxides and WO_3, xH_2O tungsten trioxide tydrates, J. Solid State Chem. 67 (1987) 235-247.

[39] A. Rougier, F. Portemer, A. Quédé, M. El Marssi. Characterization of pulsed laser deposited WO3 thin films for electrochromic devices, Appl. Surf. Sci. 153 (1999) 1-9.

[40] C. Santato, M. Odziemkowski, M. Ulmann, J. Augustynski. Crystallographically Oriented Mesoporous WO_3 Films: Synthesis, Characterization, and Applications, J. Am. Chem. Soc. 123 (2001) 10639-10649.

[41] C. Bittencourt, R. Landers, E. Llobet, X. Correig, J. Calderer. The role of oxygen partial pressure and annealing temperature on the formation of W = O bonds in thin WO_3 films, Semicond. Sci. Technol. 17 (2002) 522-525.

[42] F. Amano, M. Tian, B. Ohtani, A. Chen. Photoelectrochemical properties of tungsten trioxide thin film electrodes prepared from facet-controlled rectangular platelets, J. Solid State Electrochem. 16 (2012) 1965-1973.

[43] C. K. Wang, C. K. Lin, C. L. Wu, S. C. Wang, J. L. Huang. Synthesis and characterization of electrochromic plate-like tungsten oxide films by acidic treatment of electrochemical anodized tungsten, Electrochim. Acta 112 (2013) 24-31.

[44] S. H. Lee, H. M. Cheong, C. E. Tracy, A. Mascarenhas, D. K. Benson, S. K. Deb. Raman spectroscopic studies of electrochromic a-WO_3, Electrochim. Acta 44 (1999) 3111-3115.

[45] T. Sharifi, Y. Ghayeb, T. Mohammadi. Study of conformational changes in serum albumin by binding of chlorfenvinphos using multispectroscopic techniques and molecular dynamic simulation, Monatsh. Chem. 148 (2017) 781-791.

[46] E. Lassner and W. D. Schubert, Tungsten. Properties, Chemistry, Technology of the Element, Alloys, and Chemical Compounds, Kluwer Academic / Plenum Publishers, New York, 1999.

Tables captions

Table 1. Charge-transfer resistance values (R_1 and R_2) for the WO_3 nanostructures.

Table 2.Pseudo-first order kinetic coefficients for chlorfenvinphos degradation (k) for the different experimental conditions.

Table 3. p-values for each factor (A: Temperature; B: pH) and for the interaction between them (AB). The regression coefficients defined in equation (2) as β_0, β_1, β_2 and β_3 are also shown.

Figures captions

Figure 1. FESEM images (at 15 KX) of the formed nanostructures after the annealing treatment at different temperatures: (a) 400º C, (b) 600º C; current density transient recorded during tungsten anodization (c).

Figure 2. (a) Raman spectra of the WO_3 nanostructures after annealing at 400º C and 600º C; (b) EDX spectrum of the WO_3 nanostructure after annealing at 400º C.

Figure 3. EIS experimental results for the WO_3 nanostructures presented in the form of Nyquist (a) and Bode-phase (b) plots. The equivalent circuit used to fit these results is also shown (c).

Figure 4. Temporal evolution of chlorfenvinphos UV absorbance spectra for the different experimental conditions.

Figure 5. (a) Degradation efficiencies for the different experimental conditions; (b) TOC values for all different conditions, together with the percentage of TOC decrease.

Figure 6. Main effects (a) and interaction plots (b) for kinetic coefficient *k*.

Figure 1

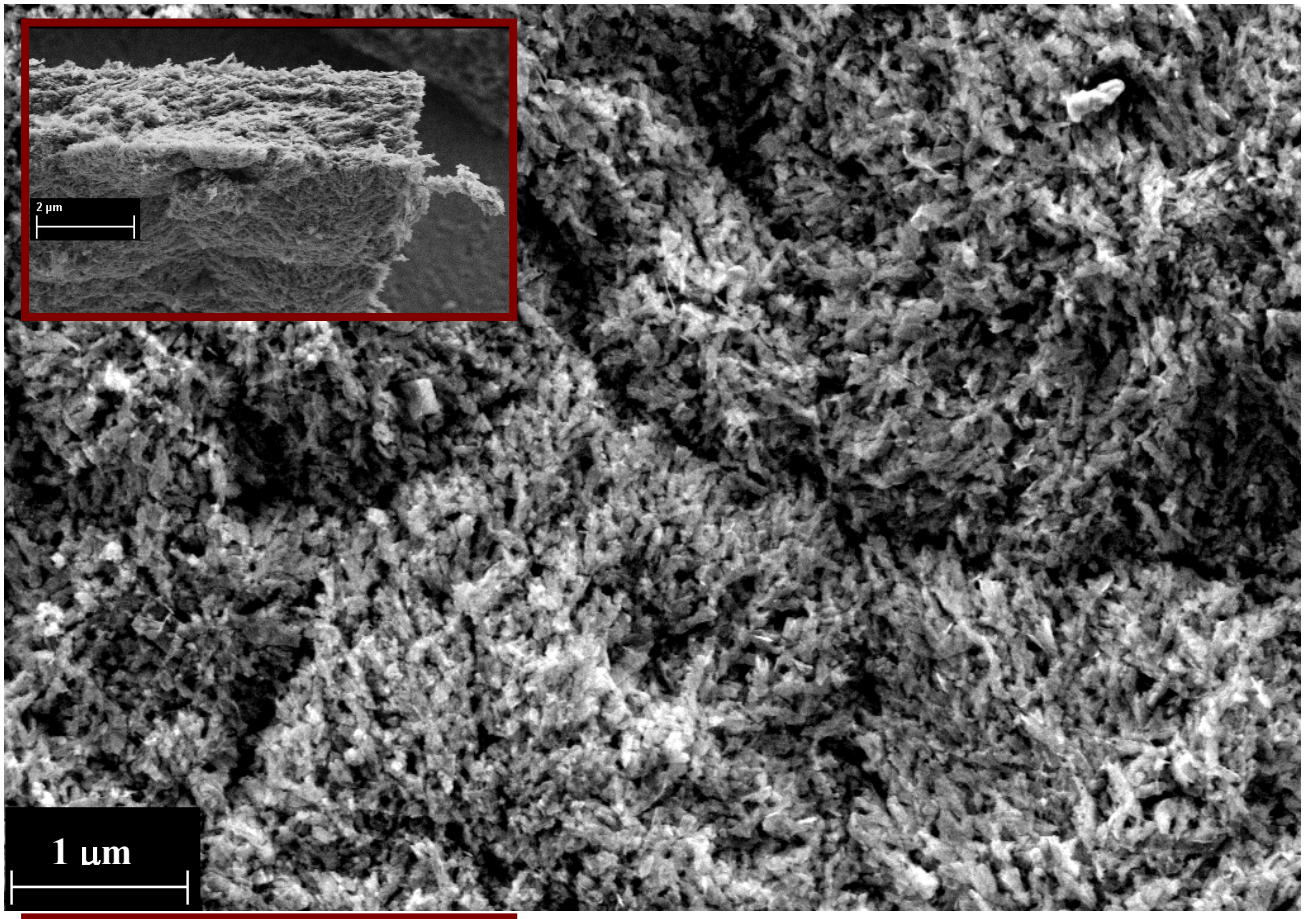

(a)

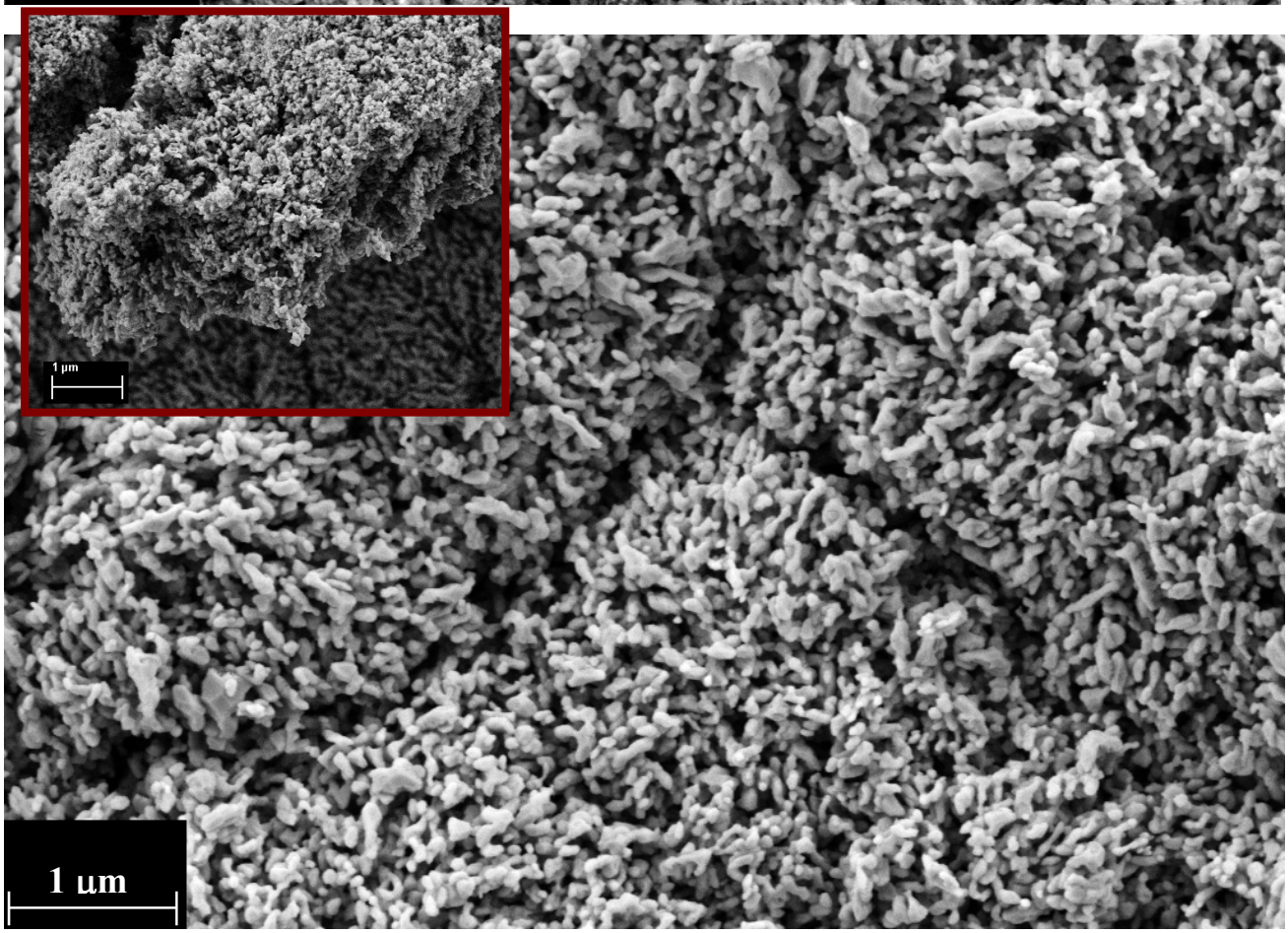

(b)

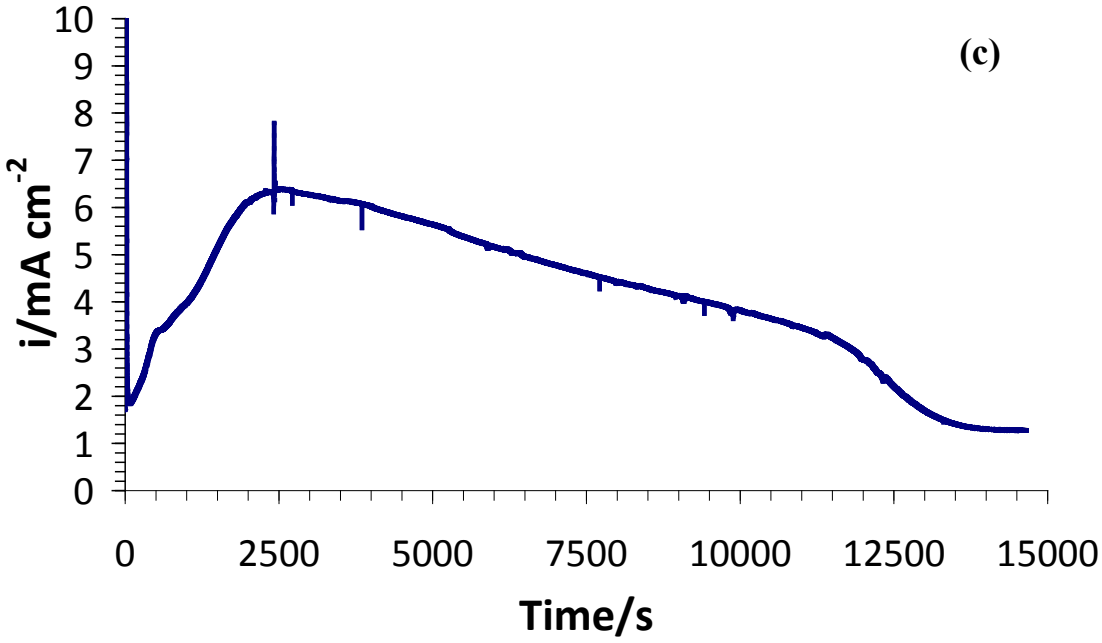
(c)
i/mA cm-2
10
9
8
7
6
5
4
3
2
1
0
0
2500
5000
7500
10000
12500
15000
Time/s

Figure 2

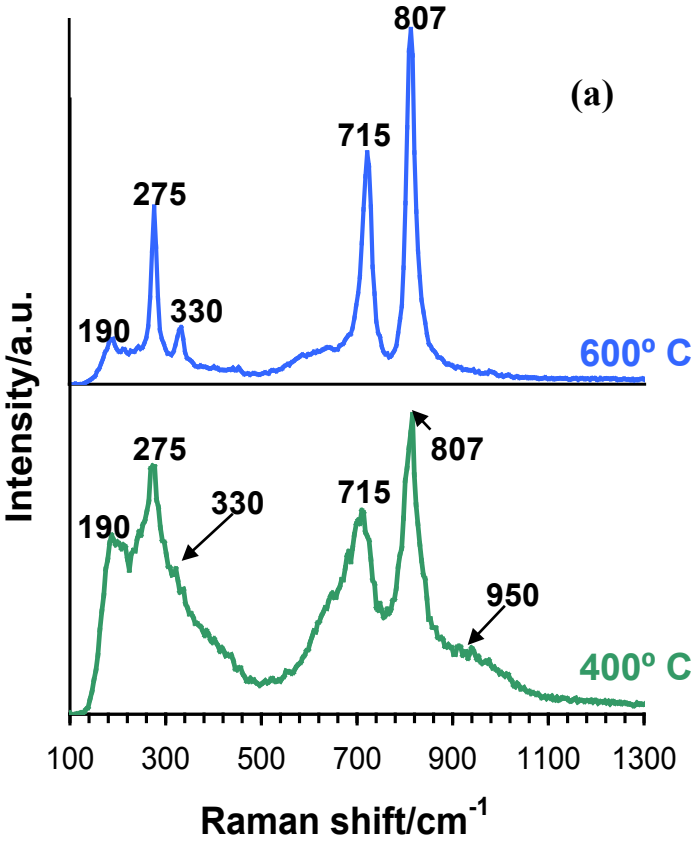
(a)
807
715
275
330
190
600º C
275
807
330
715
190
950
400º C
Intensity/a.u.
100
300
500
700
900
1100
1300
Raman shift/cm-1

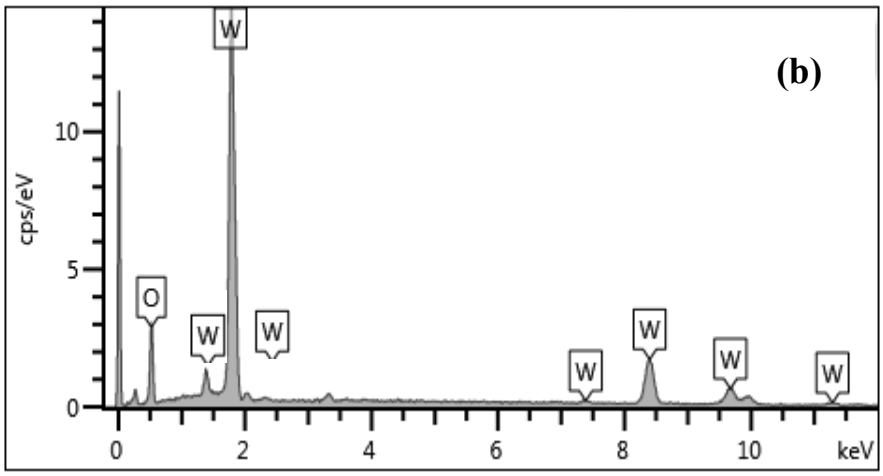
(b)
W
O
W
W
W
W
W
W
cps/eV
10
5
0
0
2
4
6
8
10
keV

Figure 3

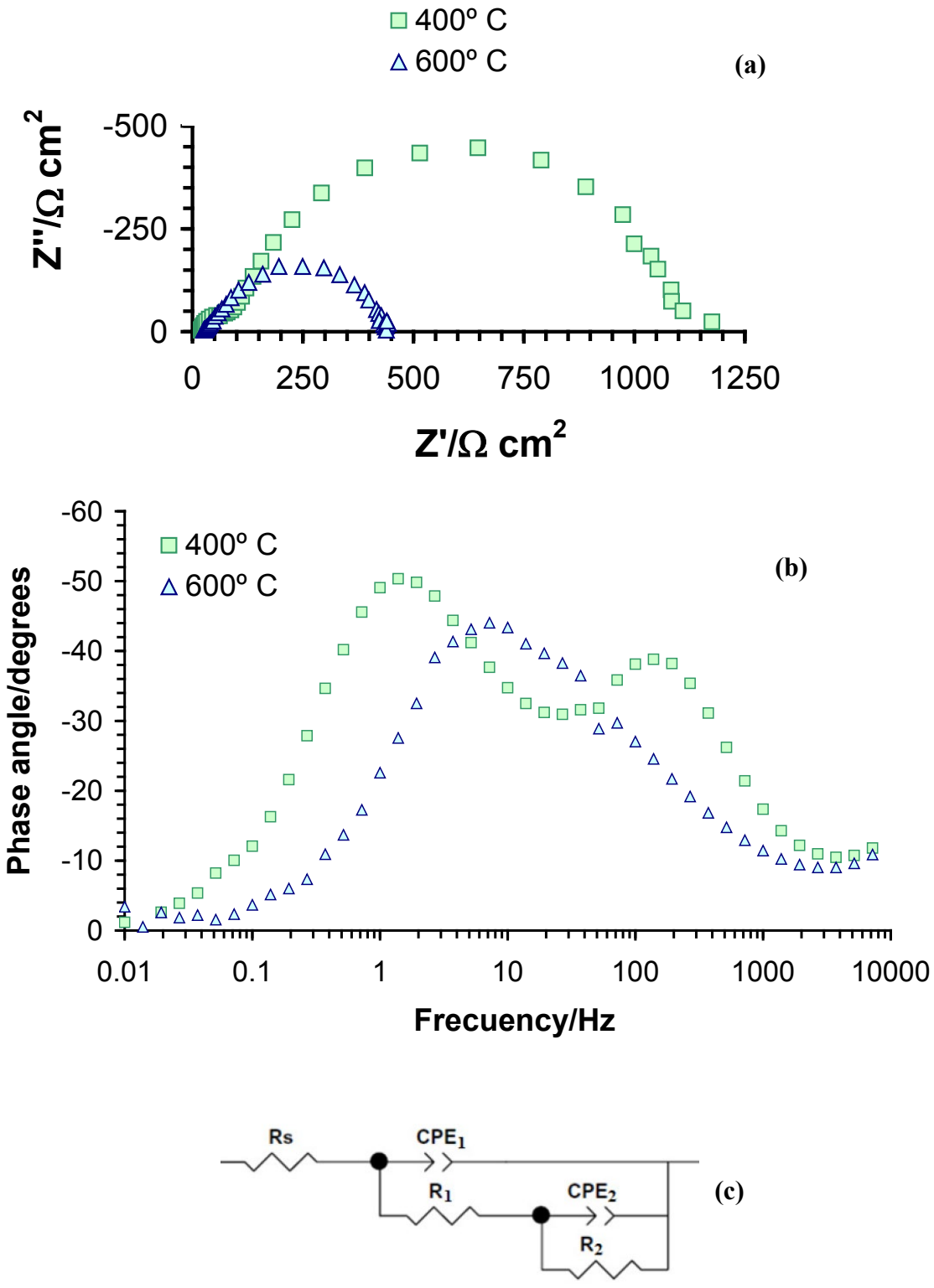
400º C
600º C
(a)
Z''/Ω cm2
-500
-250
0
0
250
500
750
1000
1250
Z'/Ω cm2
400º C
600º C
(b)
Phase angle/degrees
-60
-50
-40
-30
-20
-10
0
0.01
0.1
1
10
100
1000
10000
Frecuency/Hz
Rs
CPE1
R1
CPE2
R2
(c)

Figure 4

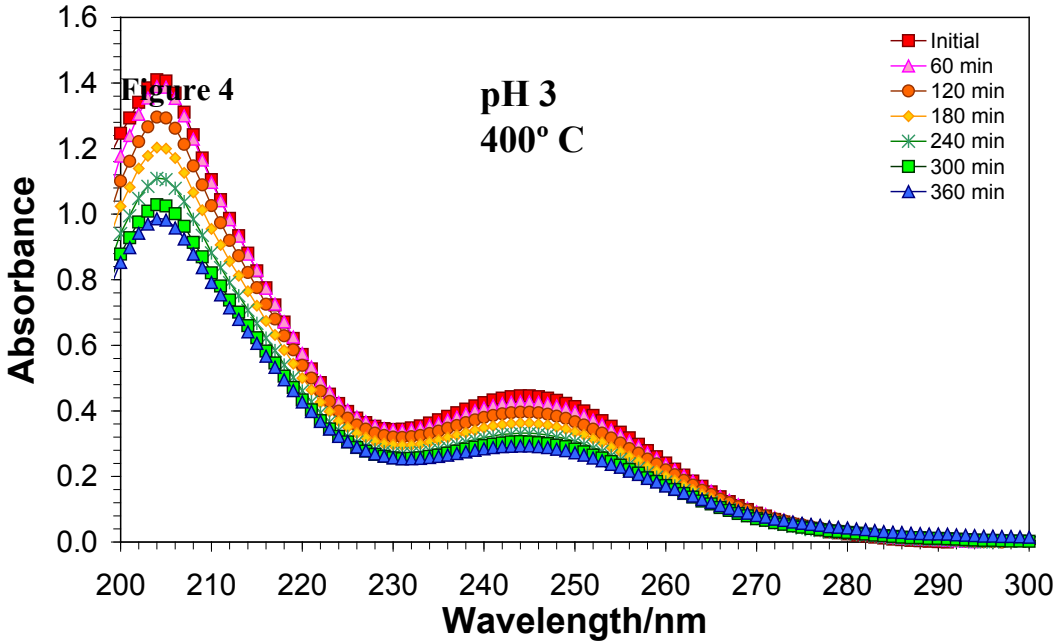
pH 3
400º C
Initial
60 min
120 min
180 min
240 min
300 min
360 min
Absorbance
Wavelength/nm

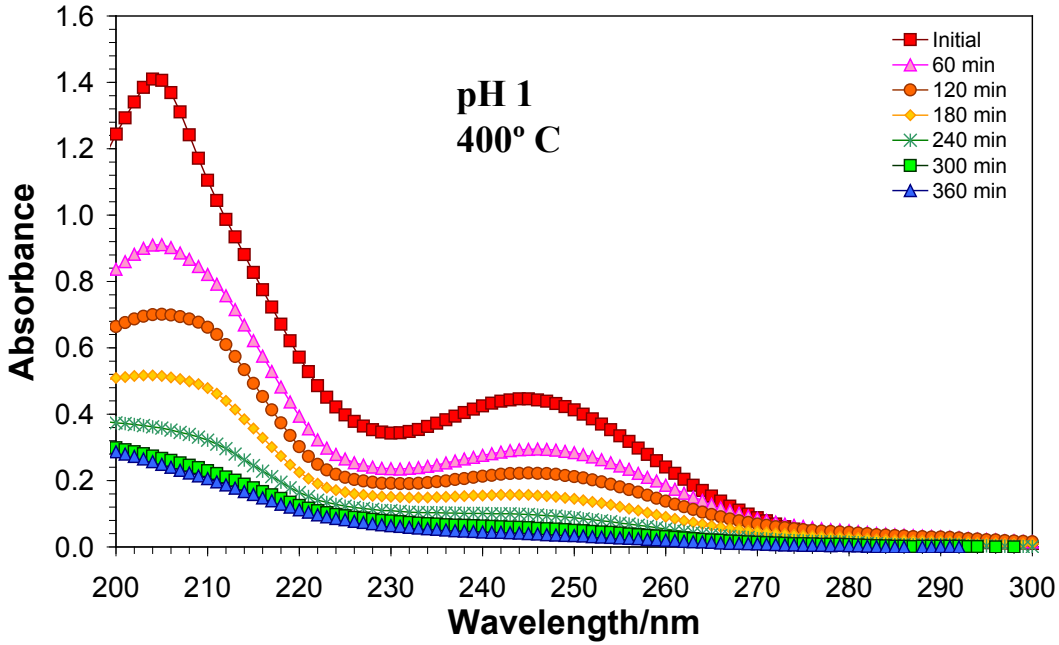
pH 1
400º C
Initial
60 min
120 min
180 min
240 min
300 min
360 min
Absorbance
Wavelength/nm

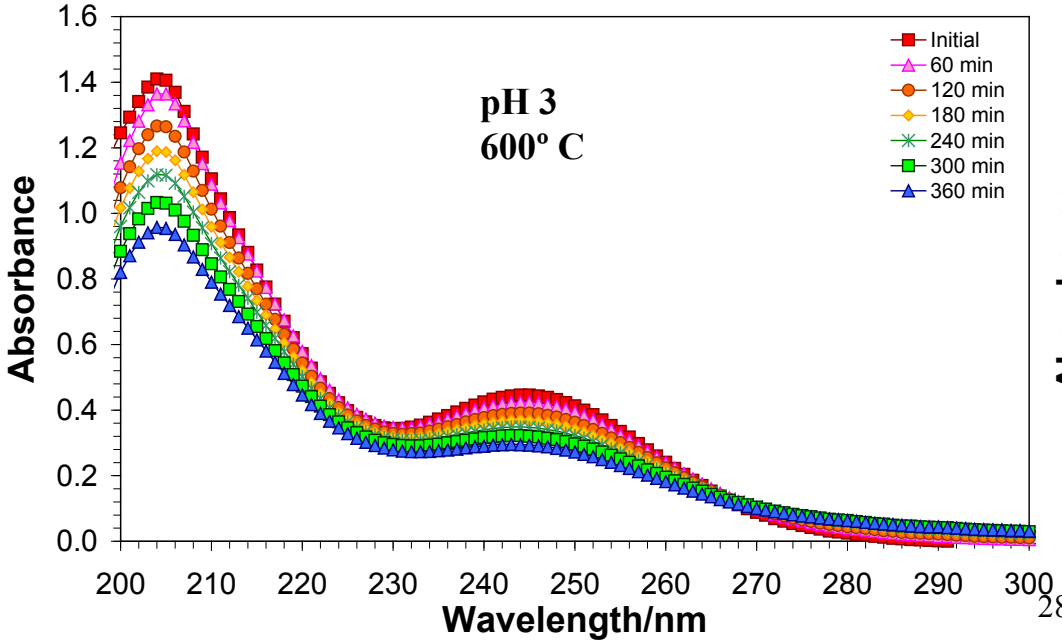
pH 3
600º C
Initial
60 min
120 min
180 min
240 min
300 min
360 min
Absorbance
Wavelength/nm

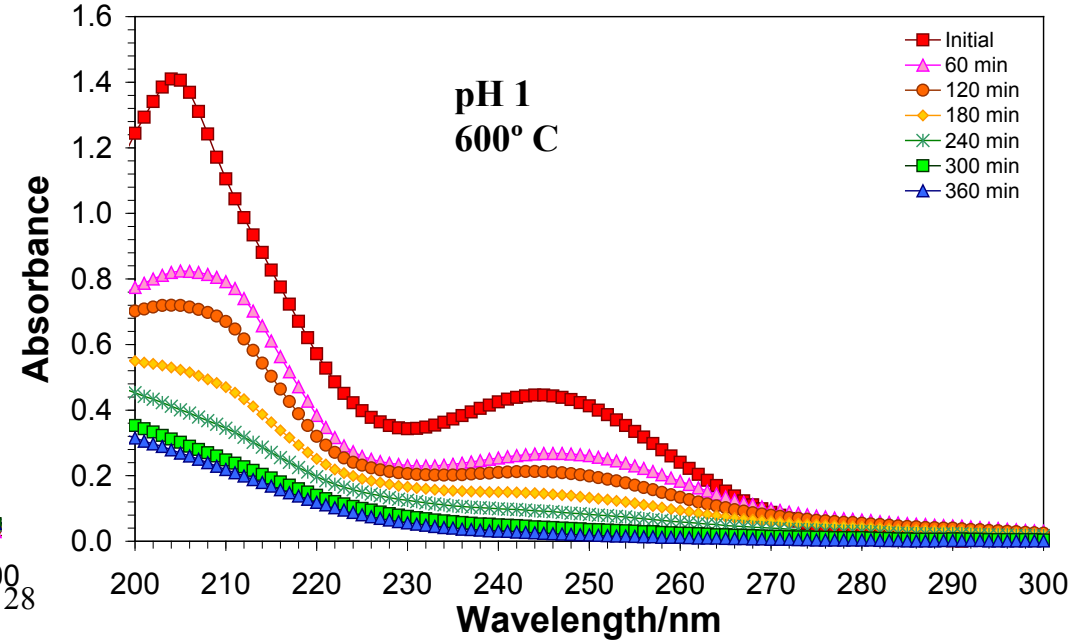
pH 1
600º C
Initial
60 min
120 min
180 min
240 min
300 min
360 min
Absorbance
Wavelength/nm

Figure 5

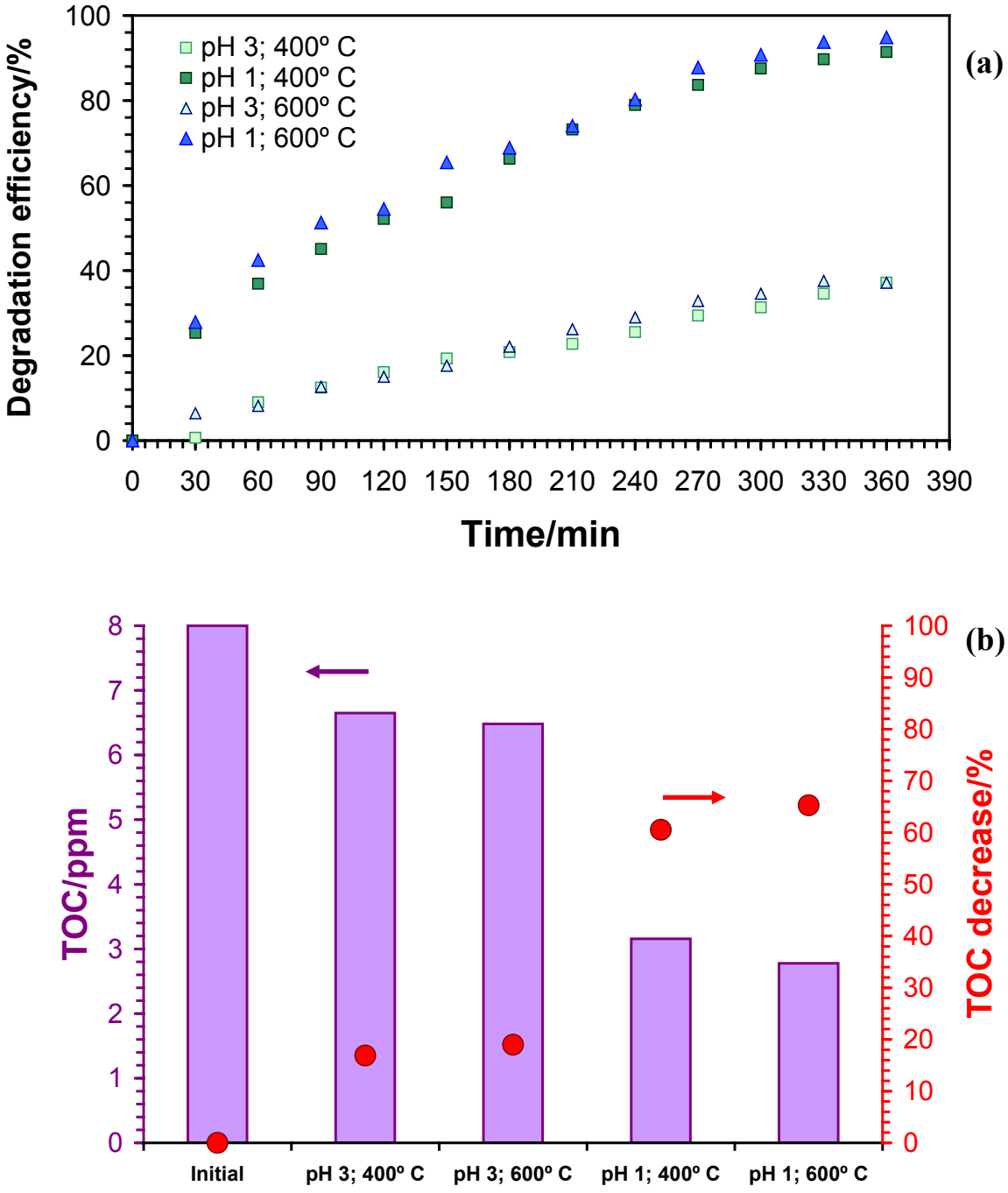
Degradation efficiency/%
Time/min
pH 3; 400° C
pH 1; 400° C
pH 3; 600° C
pH 1; 600° C
(a)
TOC/ppm
TOC decrease/%
Initial
pH 3; 400° C
pH 3; 600° C
pH 1; 400° C
pH 1; 600° C
(b)

Figure 6

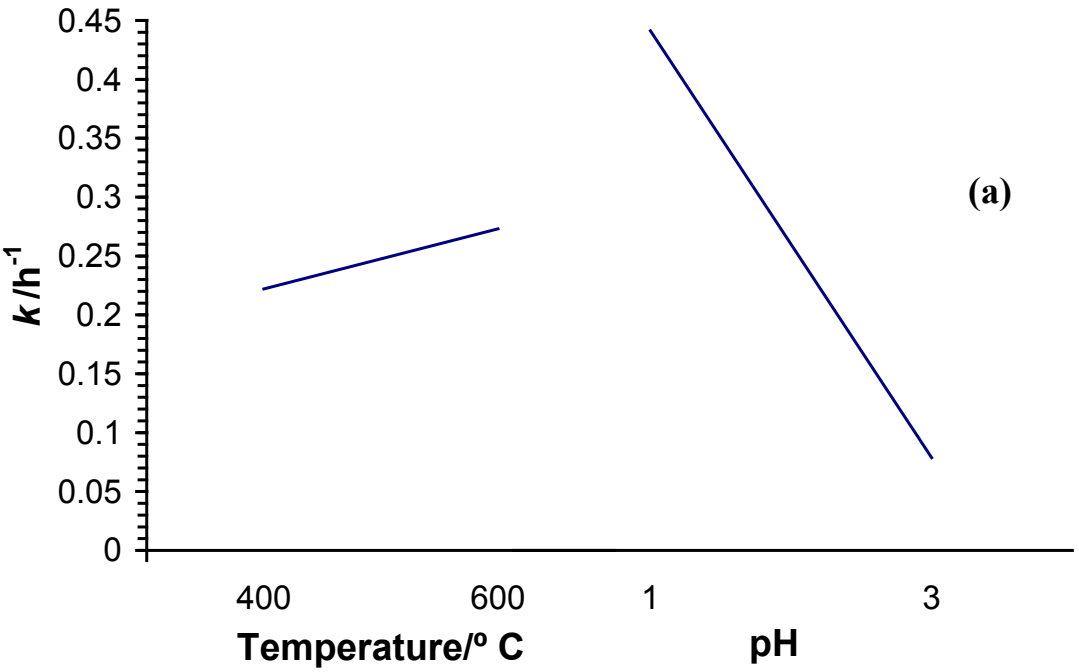
0.45
0.4
0.35
0.3
0.25
0.2
0.15
0.1
0.05
0
k /h-1
(a)
400
600
1
3
Temperature/º C
pH

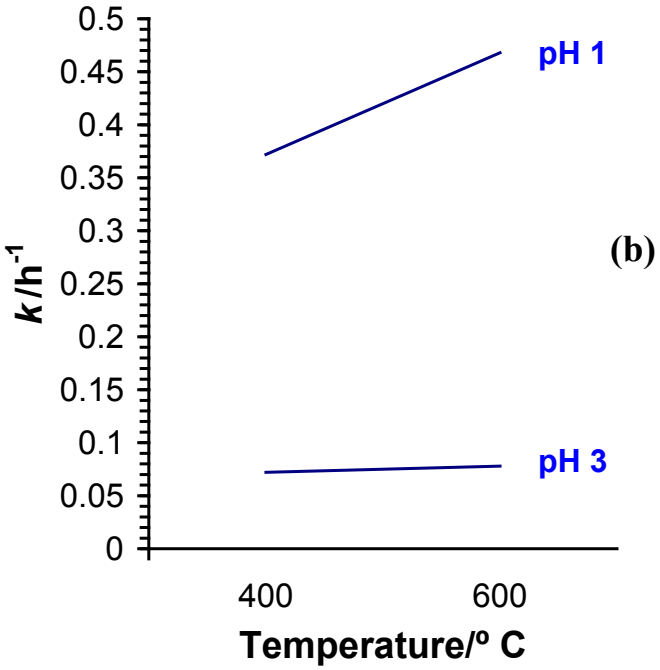
0.5
0.45
0.4
0.35
0.3
0.25
0.2
0.15
0.1
0.05
0
k /h-1
pH 1
(b)
pH 3
400
600
Temperature/º C

Table 1

WO_3 sample	*R_1*/Ω cm^2	*R_2*/Ω cm^2
400º C	109 ± 8	991 ± 34
600º C	42 ± 7	378 ± 16

Table 2

Temperature/º C	pH	*k*/min^{-1}	*k*/s^{-1} (x10^{-5})	R^2
400	3	0.0012	2.0	0.989
400	1	0.0062	10.3	0.989
600	3	0.0013	2.2	0.988
600	1	0.0078	13	0.971

Table 3

Effect	*p*-value	Regression coefficient (x10^{-5}; *k* in min^{-1})
-----	-----	$\beta_0 = 400$
A: Temperature	$<10^{-4}$	$\beta_1 = 1.175$
B: pH	$<10^{-4}$	$\beta_2 = -100$
AB	$<10^{-4}$	$\beta_3 = -0.375$